APL Materials

RESEARCH ARTICLE | JULY 20 2023

Thermodynamic route of Nb_3Sn nucleation: Role of oxygen

Zeming Sun ✉ ; Darrah K. Dare ; Zhaslan Baraissov ; David A. Muller ; Michael O. Thompson ;
Matthias U. Liepe

APL Mater. 11, 071118 (2023)
https://doi.org/10.1063/5.0157659

AIP Publishing

APL Materials ARTICLE pubs.aip.org/aip/apm

Thermodynamic route of Nb_3Sn nucleation: Role of oxygen

Cite as: APL Mater. 11, 071118 (2023); doi: 10.1063/5.0157659
Submitted: 9 May 2023 • Accepted: 7 July 2023 •
Published Online: 20 July 2023

Zeming Sun,[1,a)] Darrah K. Dare,[2] Zhaslan Baraissov,[3] David A. Muller,[3] Michael O. Thompson,[4] and Matthias U. Liepe[1]

AFFILIATIONS

[1] Cornell Laboratory for Accelerator-Based Sciences and Education, Cornell University, Ithaca, New York 14853, USA
[2] Cornell Center for Materials Research, Cornell University, Ithaca, New York 14853, USA
[3] School of Applied and Engineering Physics, Cornell University, Ithaca, New York 14853, USA
[4] Materials Science and Engineering, Cornell University, Ithaca, New York 14853, USA

[a)] Author to whom correspondence should be addressed: zs253@cornell.edu

ABSTRACT

Intermetallic Nb_3Sn alloys have long been believed to form through Sn diffusion into Nb. However, our observations of significant oxygen content in Nb_3Sn prompted an investigation of alternative formation mechanisms. Through experiments involving different oxide interfaces (clean HF-treated, native oxidized, and anodized), we demonstrate a thermodynamic route that fundamentally challenges the conventional Sn diffusion mechanism for Nb_3Sn nucleation. Our results highlight the critical involvement of a SnO_x intermediate phase. This new nucleation mechanism identifies the principles for growth optimization and new synthesis of high-quality Nb_3Sn superconductors.

I. INTRODUCTION

Nb_3Sn[1–3] is a crucial and promising superconductor that finds widespread applications in various modern technologies, including superconducting radio-frequency (SRF) resonators,[4–6] high-field magnets,[7] and emerging electronics, such as quantum devices and high-capability detectors.[8] Of particular interest are SRF resonant cavities that accelerate charged particle beams by coupling RF superconductors with RF waves. These cavities are critical components for modern particle accelerators, with applications spanning from photon science,[9–11] high-energy and nuclear physics,[12,13] advanced materials discovery,[9,10] isotope production,[14] to quantum computing.[15]

For SRF applications, Nb_3Sn possesses advantages over the conventional material niobium (Nb). Nb_3Sn exhibits a high predicted superheating field (400 mT), twice that of Nb (200 mT), allowing for large accelerating gradients up to 100 MV/m.[16] Nb_3Sn has a higher critical temperature (T_c) of 18 K compared to Nb's 9.2 K, resulting in lower surface resistance and higher quality factors. The higher T_c of Nb_3Sn enables the replacement of costly helium cryogenics (operated at 2 K) with commercial cryocoolers (operated at 4.2 K), thereby facilitating the development of turn-key, compact accelerators.[17] With excellent capabilities, Nb_3Sn-based cavities are poised to advance toward practical accelerator applications.[18]

To date, efficient SRF cavities that utilize Nb_3Sn films are dominantly produced through tin (Sn) vapor diffusion on Nb surfaces.[18–21] Recently, a new process involving Sn electroplating on Nb followed by thermal annealing has been demonstrated,[22] with other methods, e.g., sputtering, being explored.

The vapor diffusion process for synthesizing Nb_3Sn involves heating Nb in the presence of vaporized Sn at ~500 °C for ~4 h for nucleation, followed by heating at ~1100 °C for 2–3 h for grain growth. To optimize the process, various improvements have been implemented, including switching from native Nb-oxidized surfaces to anodized surfaces and from the pure Sn source to an additional high-vapor-pressure $SnCl_2$ source. Regardless of these changes, the observation of thick oxides and high subsurface oxygen concentrations in vapor-diffused Nb_3Sn[22,23] has raised questions about the source of oxygen during nucleation.

Since the 1980s, the proposed mechanism for intermetallic formation of Nb_3Sn has been based on the diffusion of Sn through the grain boundary of Nb or an initially nucleated thin interface of Nb_xSn_y. This leads to further growth of Nb_3Sn or Nb_xSn_y and slow bulk diffusion to produce Nb_3Sn.[24,25] Recent atomic simulations have confirmed that grain boundary diffusion in Nb_3Sn is significantly faster than bulk diffusion, e.g., 10^5 times faster at 1100 °C.[26,27] This diffusion-based mechanism has been widely used to analyze and optimize Nb_3Sn growth.[20,28–31]

The early stage of Nb_3Sn nucleation has been investigated using the Sn vapor process.[29–31] This study stands apart from previous research in several ways, challenging existing assumptions.

First, previous investigations followed the assumption that Sn is the primary component involved in the nucleation process and identified a pure kinetic problem to address non-uniform nucleation issues. However, this work reveals that the thermodynamic route actually involves an intermediate phase of SnO_x in the nucleation process.

Second, vapor-based investigations observed the formation of droplet regions, likely representing the initial nuclei.[29–31] However, accurate identification of these droplets remains unverified due to several challenges in characterization. Electron dispersive spectroscopy analysis of these droplets is plagued by unreliable measurements caused by interference from oxygen signals. Cross-sectional transmission electron microscopy imaging poses challenges: sample preparation involving focused ion beam polishing under 5×10^{-7}–10^{-6} Torr introduces errors related to the presence of residual oxygen in the chamber; the presence of non-crystalline oxides further complicates the identification of these nuclei.

Here, we design the sample architectures to ensure a good capping of the interface between the precursor $SnCl_2$ and the substrate, preventing exposure to air. Probing the interface using X-ray photoelectron spectroscopy (XPS) depth profiling under 10^{-10}–10^{-9} Torr provides semi-*in situ* identification of the nuclei with more reliable results to date.

II. EXPERIMENTAL SECTION

Three different layouts of $SnCl_2/(Nb_xO_y)/Nb$ were fabricated: (i) a clean Nb surface treated with hydrofluoric acid (HF) followed by $SnCl_2$ deposition ($SnCl_2/Nb$); (ii) a native oxidized surface comprising a ~7 nm oxide stack[23] followed by $SnCl_2$ deposition ($SnCl_2$/thin, native oxide/Nb); and (iii) an anodized surface with a 60 nm-thick, porous oxide layer followed by $SnCl_2$ deposition ($SnCl_2$/thick, porous oxide/Nb).

High-purity Nb substrates were used with a large grain size of > 50 mm and a residual-resistivity ratio of >300. The 1×1 cm^2 substrates were electropolished using a mixture of 1:9 HF (48%) and sulfuric (98%) acids, resulting in an average surface roughness of 40 nm after a 100 μm polishing. The anodization process utilized the electropolished Nb as the anode and Pt as the cathode in a two-electrode control. The solution used was concentrated sodium hydroxide, and the voltage applied was up to 30 V, producing porous oxides as imaged by scanning electron microscope (SEM) in Fig. 1(a).

Afterward, the substrates were transferred to a nitrogen-flown glovebox with O_2 and H_2O levels below 0.5 ppm, and all subsequent operations were performed in the glovebox. One type of substrate was soaked in 2% HF for 30 min and dried. $SnCl_2$ dihydrate microparticles were dissolved in methanol at a concentration of 1 mg/ml. The drop casting technique was employed to deposit 2 ml of $SnCl_2$ solution onto the substrate surface, followed by solvent evaporation. Uniform coverage of white films was observed on the anodized sample, while it took several attempts to obtain comparable coverage for the other two conditions, which showed poor adhesion.

Following baseline characterizations, the samples underwent annealing in a Lindberg tube furnace under a vacuum of 5×10^{-7} Torr at 300 °C for 4 h. While this temperature is lower than the typical nucleation temperature for vapor diffusion (500 °C for 4 h under ~10^{-6} Torr), it was chosen to capture the early stages of transformation.

Chemical states, elemental compositions, and phase structures were determined using X-ray photoelectron spectroscopy (XPS) with depth profiling and high-resolution X-ray diffraction (XRD). To accommodate thick films reaching up to 30 μm, XPS survey scans were performed with sputtering intervals ranging from 1 to 327 nm using a Surface Science Instruments SSX-100 ESCA spectrometer. Monochromatic Al k-alpha X-ray (1486.6 eV) photoelectrons were collected from an 800 μm analysis spot at a 55° emission angle under a vacuum of 10^{-9} Torr. The scan parameters were set to 150 eV pass energy, 1 eV step size, and 100 s/step. For depth profiles, a 4 kV Ar^+ beam with a spot size of ~5 mm was rastered over a 2×4 mm^2 area.

Phase structures were further analyzed using a Rigaku SmartLab XRD instrument. The X-ray generated by a Cu target was converted into a parallel, monochromatic beam and directed onto the sample surface after passing through a 5 mm divergence slit. The $K\alpha$ signal with a wavelength of 0.154 nm was collected by filtering the diffracted beam. The parallel slit analyzer and 5° Soller slits were used to resolve high-resolution signals. The 2θ scan was performed with a step size of 0.0032°.

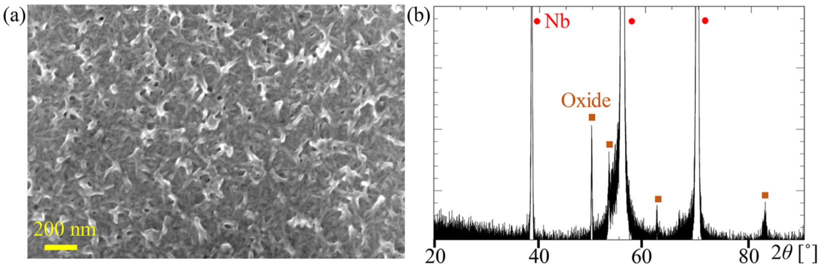

FIG. 1. (a) SEM surface image and (b) XRD pattern of the anodized Nb.

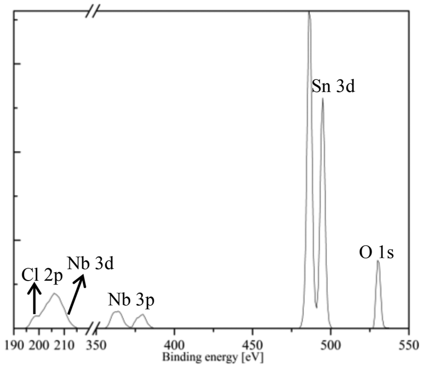

FIG. 2. XPS spectra for the anodized sample after 300 °C annealing, taken at a depth of 200 nm. The intensity units are arbitrary.

III. RESULTS

To gain insight into the structural changes and reactions between multiple elements, XPS spectra of Sn 3d, Nb 3p, O 1s, and Cl 2p (e.g., Fig. 2) were collected as a function of depth for the as-deposited and 300 °C annealed samples. The binding energies are determined with reference to Table I. To accurately interpret the results, we combine the information from concentration profiles (Fig. 3), FWHM (full-width-at-half-maximum) changes (Fig. 4), and binding energy shifts (Fig. 5), while accounting for the sputtering effects and resolution challenges.

A. As-deposition

The oxygen-free interface on clean Nb [Fig. 3(a)] shows the appearance of $NbCl_x$ and Nb_xSn_y following $SnCl_2$ deposition. Incorporation of these two new Nb and Sn structures results in FWHM increases up to 6.5 and 4.5 eV, respectively (Fig. 4). The 485 eV Sn binding energy strongly indicates the generation of Nb_xSn_y alloying upon deposition [Fig. 5(a)]. The 365 eV Nb binding energy is attributed to $NbCl_x$ [Fig. 5(b)], as no oxygen signals were detected, ruling out the possibility of Nb oxides that have characteristic peaks in the same positions.

In contrast, the presence of oxygen in the native oxidized and anodized interfaces causes a clear disappearance of chlorine [Figs. 3(b) and 3(c)]. The formation of $NbCl_x$ and Nb_xSn_y is still observed, as evidenced by the similar FWHM spikes (Fig. 4) and characteristic binding energies [Figs. 5(a) and 5(b)].

B. After 300 °C annealing

Figures 3(d)–3(f) demonstrate the absence of chlorine and the conversion into Sn oxides. To support the phase identification,

TABLE I. Binding energies (eV) of relevant motifs in the literature.[23,32–35]

Sn $3d_{5/2}$	484–485 (metallic)	486–487 (SnO/SnO_2)	488 ($SnCl_2$)	491.2 (charging)
Nb $3p_{3/2}$	360.5–361 (metallic)	363–365 (Nb oxides)	365 ($NbCl_5$)	
O 1s	529.5–530.5 (oxides)	532–534 (hydroxides)	> 537 (charging)	
Cl $2p_{3/2}$	198.5–199.5 (chlorides)			

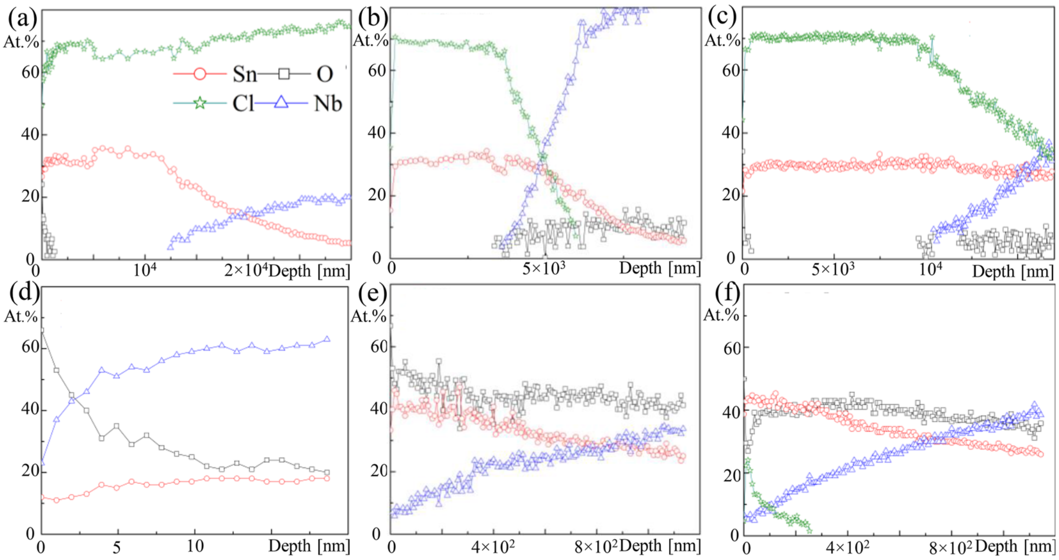

FIG. 3. Atomic concentrations of Sn, Nb, O, and Cl as a function of depth for the as-deposited [(a)–(c)] and annealed [(d)–(f)] samples. [(a) and (d)] Clean Nb, [(b) and (e)] native oxidized, and [(c) and (f)] anodized. The concentration uncertainty is <5%. The depth resolution is affected by the sputtering effect.

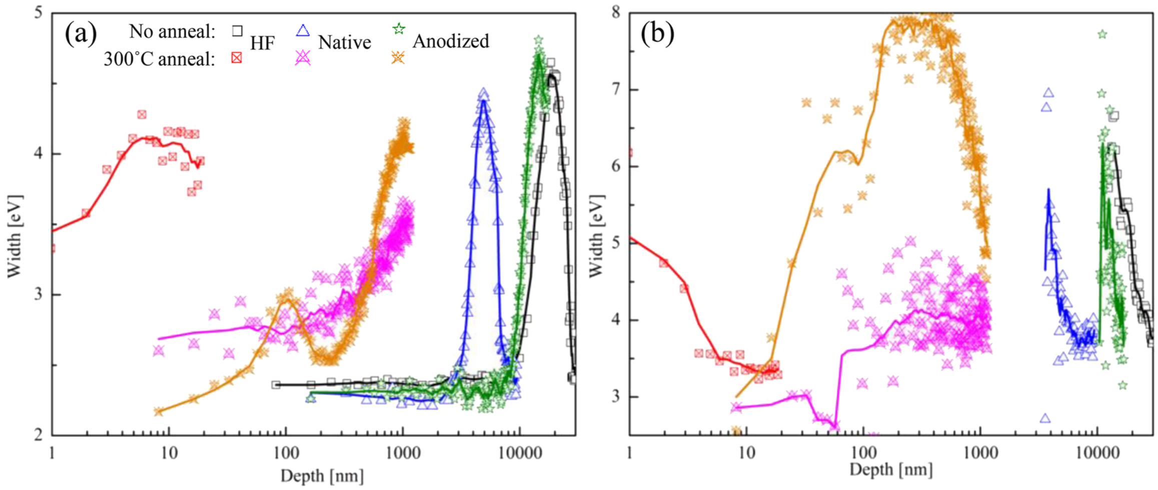

FIG. 4. XPS peak FWHM of (a) Sn $3d_{5/2}$ and (b) Nb $3p_{3/2}$ as a function of depth, with an intrinsic width limit of ~2.3 eV.

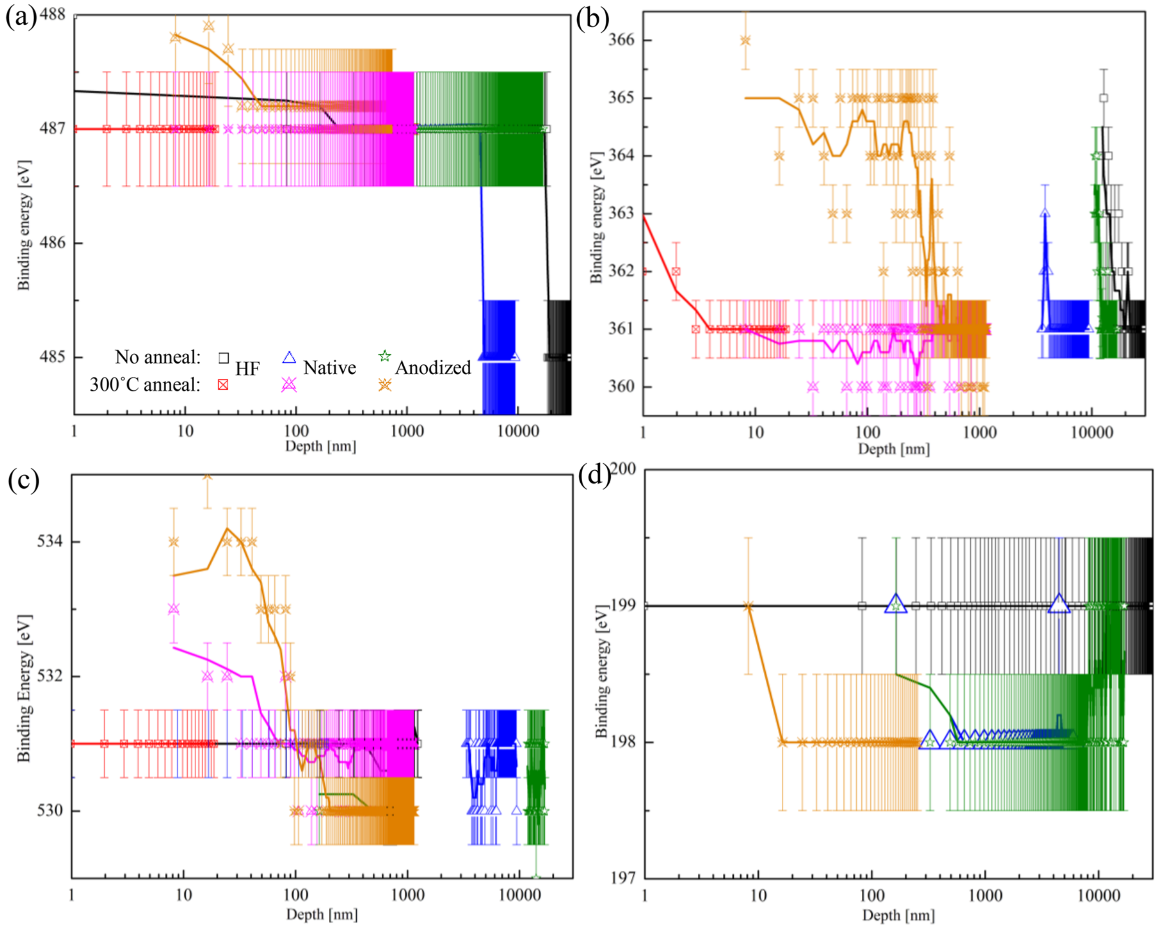

FIG. 5. XPS binding energies for (a) Sn $3d_{5/2}$, (b) Nb $3p_{3/2}$, (c) O 1s, and (d) Cl $2p_{3/2}$, plotted as a function of depth. The error bars represent a conservative uncertainty estimate of 1 eV.

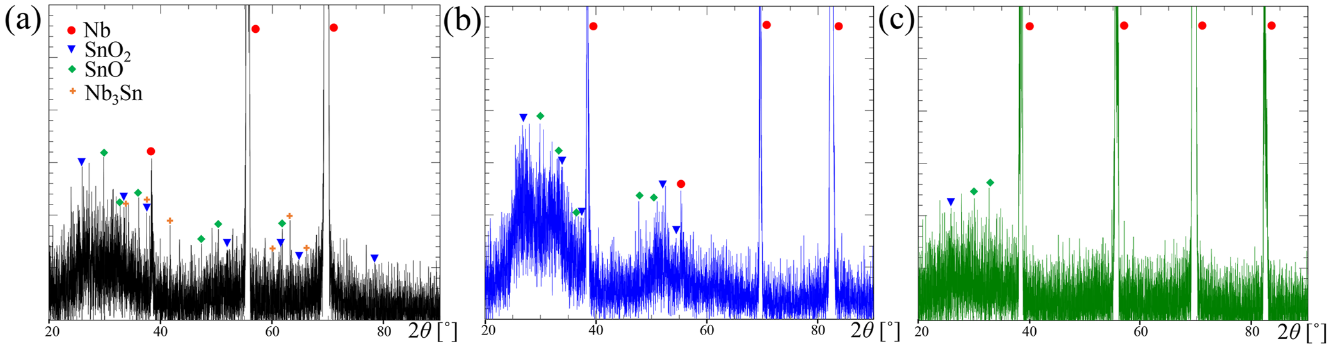

FIG. 6. High-resolution XRD patterns for the 300 °C annealed samples: (a) clean Nb, (b) native oxidized, and (c) anodized. The data were processed using the GENPLOT smoothing algorithm.

TABLE II. XRD diffraction angles for Nb ($Im\bar{3}m$), SnO_2 ($P4_2/mnm$), SnO($P4/nmm$), and Nb_3Sn ($Pm\bar{3}n$) in the database.[36]

Nb	38.4° [110]	55.4° [200]	69.4° [211]	82.2° [220]			
SnO_2	26.4° [110]	33.7° [101]	38.7° [111]	51.5° [211]	54.5° [220]	57.5° [002]	61.5° [310]
	64.3° [112]	71.4° [320]	78.2° [321]				
SnO	29.7° [101]	33.2° [110]	36.8° [002]	47.7° [200]	50.4° [112]	57.2° [211]	61.9° [103]
Nb_3Sn	33.7° [200]	37.8° [210]	41.5° [211]	60.2° [320]	62.9° [320]	70.78° [400]	

high-resolution XRD patterns are presented in Fig. 6 and referenced in Table II.

The clean Nb sample, with a Sn concentration of ~10 at. % and a thinness of ~10 nm, exhibits the lowest amount of SnO_x [Fig. 5(a)]. On the surface, higher-order Nb oxides of ~3 nm are present. Underneath this layer, metallic Nb [Fig. 5(b)] is mixed with SnO_x, resulting in increased Sn FWHM and decreased Nb FWHM (Fig. 4). A low amount of Nb_xSn_y may be present, as suggested in the XRD pattern [Fig. 6(a)], but the characteristic peak of metallic Sn is not prominent. The rapid decrease in oxygen concentration within ~5 nm for this condition suggests the source of oxygen should be the residual gas in the furnace chamber with a vacuum of 5×10^{-7} Torr, which differs from the two oxidized samples where oxygen is evenly distributed at 50 at. % throughout the samples.

The native and anodized samples with initial oxides exhibit similarity in the concentration profile [Figs. 3(e) and 3(f)]. Both conditions yield significant amounts of SnO_x in addition to Nb_xSn_y nuclei, as evidenced by the persistence of Sn binding energies at 487 eV associated with SnO_x [Fig. 5(a)] and the observed diffraction patterns of SnO_2 and SnO [Figs. 6(b) and 6(c)]. Nb_xSn_y starts to emerge at a depth of ~200 nm, as indicated by the considerably broadened width of both Sn and Nb XPS peaks in Fig. 4. These results provide compelling evidence that SnO_x is a necessary intermediate phase for alloying.

Nevertheless, the anodized sample differs from the native oxidized sample due to the presence of residual $SnCl_2$ on the surface [Figs. 3(f) and 5(d)], resulting in a higher Sn binding energy [Fig. 5(a)] and a width spike in the Sn peak [Fig. 4(a)] at the < 200 nm surface. Within the same depth range, the anodized oxides persist and convert to a larger quantity of higher-order oxides, as evidenced by the 365 eV binding energies [Fig. 5(b)] and the largest Nb peak width with all charge states [Fig. 4(b)]. The adoption of anodization for vapor diffusion produces a smoother Nb_3Sn surface. Our data suggest that the underlying mechanisms involve two aspects: (i) a larger and more uniform adsorption of $SnCl_2$ due to the porous oxide structures, as shown in Fig. 3(c), and (ii) a prolonged reaction time with additional $SnCl_2$ source at a later stage and additional Nb oxides for producing the intermediate SnO_x phases necessary for generating the intermetallic alloy.

IV. DISCUSSION

The early stage of Nb_xSn_y nucleation (e.g., at 300 °C) crucially determines the quality of the final Nb_3Sn product, especially in applications involving vapor diffusion in SRF cavities. Achieving a smooth surface in Nb_3Sn relies on the uniformity of the initial nuclei, which serve as a seed layer for promoting uniform grain growth. Moreover, $Nb_{3-n}Sn$ has stoichiometric boundaries of 18 and 25 at. % Sn, with the desired stoichiometry of 25 at. % Sn corresponding to the critical temperature limit of 18 K. Correcting the nucleation from an initial 18 at. % stoichiometry to the desired 25 at. % is challenging. Previous nucleation studies assumed Sn to be the main component involved, considering it to be a purely kinetic problem dependent on the availability of sufficient Sn supply.[29–31] However, our observations challenge the application of this assumption to the *nucleation* process, while it remains unclear to what extent pure Sn diffusion, without the assistance of oxygen, contributes to subsequent grain growth.

Our findings reveal the critical and dominant involvement of SnO_x as a significant intermediate step during the early nucleation stage of Nb_xSn_y. Our experimental design has addressed several confusions related to nucleation during vapor diffusion while minimizing uncertainties associated with previous studies. The results directly clarify previous observations of nuclei-like droplet features, providing clear evidence that these features are not Sn droplets, but rather SnO_x entities that contain converted Nb_xSn_y. This rectifies several proposed reactions that aimed to balance the formulas with Sn as the end product, e.g., in Ref. 31. In future work, thermodynamic considerations should be prioritized, and models for SnO_x/Nb and SnO_x/NbO_x should be constructed in experiments and simulations.

These findings also explain the high oxygen content that remains in the final Nb_3Sn product. Moreover, while investigating grain growth in Nb_3Sn is beyond the scope of this study, the connection between the high oxygen content in Nb_3Sn and the involvement of SnO_x implies that oxygen is highly likely involved in the grain growth process. This point should be further verified.

Furthermore, in addition to providing insights into vapor diffusion, this work has the potential to open up new avenues for generating Nb_3Sn, moving beyond vapor diffusion.

V. CONCLUSION

To summarize, this work demonstrates the thermodynamic route for Nb_3Sn nucleation. Our results reveal the crucial role of a SnO_x intermediate phase, leading to alloy nucleation. This mechanism is particularly pronounced at the native oxidized and anodized interfaces, as well as clean Nb interfaces due to residual oxygen in the annealing vacuum furnace (5×10^{-7} Torr). Our results also suggest the anodized surfaces that produce smoother Nb_3Sn rely on increasing the quantity and even distribution of adsorbed $SnCl_2$, and enhancing the reaction kinetics through excessive $SnCl_2$ and Nb oxide sources. These insights into the nucleation mechanisms of intermetallic Nb_3Sn alloys will guide the development of optimized growth processes and new synthesis recipes for producing high-quality Nb_3Sn superconductors.

ACKNOWLEDGMENTS

This work was supported by the U.S. National Science Foundation under Award No. PHY-1549132, the Center for Bright Beams. This work made use of the Cornell Center for Materials Research Shared Facilities which are supported through the NSF MRSEC program (Grant No. DMR-1719875).

AUTHOR DECLARATIONS

Conflict of Interest

The authors have no conflicts to disclose.

Author Contributions

Zeming Sun: Conceptualization (lead); Data curation (lead); Formal analysis (lead); Investigation (lead); Methodology (lead); Validation (lead); Writing – original draft (lead); Writing – review & editing (lead). **Darrah K. Dare**: Investigation (equal); Methodology (supporting); Writing – review & editing (equal). **Zhaslan Baraissov**: Investigation (supporting); Methodology (supporting). **David A. Muller**: Funding acquisition (supporting); Project administration (supporting); Supervision (supporting). **Michael O. Thompson**: Formal analysis (supporting); Investigation (supporting); Methodology (supporting); Writing – review & editing (supporting). **Matthias U. Liepe**: Investigation (equal); Methodology (supporting); Project administration (lead); Supervision (lead); Writing – review & editing (supporting).

DATA AVAILABILITY

The data that support the findings of this study are available from the corresponding author upon reasonable request.

REFERENCES

[1] A. Godeke, "A review of the properties of Nb_3Sn and their variation with A15 composition, morphology and strain state," Supercond. Sci. Technol. **19**, R68 (2006).

[2] H. Devanta *et al.*, "The physical and structural properties of superconducting A15-type Nb-Sn alloys," J. Mater. Sci. **16**, 2145 (1981).

[3] D. F. Moore *et al.*, "Energy gaps of the A-15 superconductors Nb_3Sn, V_3Si, and Nb_3Ge measured by tunneling," Phys. Rev. B **20**, 2721 (1979).

[4] J. Zmuidzinas, "Superconducting microresonators: Physics and applications," Annu. Rev. Condens. Matter Phys. **3**, 169 (2012).

[5] H. S. Padamsee, "Superconducting radio-frequency cavities," Annu. Rev. Nucl. Part. Sci. **64**, 175 (2014).

[6] S. Posen and D. L. Hall, "Nb_3Sn superconducting radiofrequency cavities: Fabrication, results, properties, and prospects," Supercond. Sci. Technol. **30**, 033004 (2017).

[7] X. Xu, "A review and prospects for Nb_3Sn superconductor development," Supercond. Sci. Technol. **30**, 093001 (2017).

[8] S. M. Anlage, "Microwave superconductivity," IEEE Microwave. Mag. **1**, 389 (2021).

[9] P. G. O'Shea and H. P. Freund, "Free-electron lasers: Status and applications," Science **292**, 1853 (2001).

[10] B. W. J. N. R. Thompson and N. R. Thompson, "X-ray free-electron lasers," Nat. Photonics **4**, 814 (2010).

[11] N. Huang *et al.*, "Features and futures of X-ray free-electron lasers," Innovation **2**, 100097 (2021).

[12] C. E. Reece, "Continuous wave superconducting radio frequency electron linac for nuclear physics research," Phys. Rev. Accel. Beams **19**, 124801 (2016).

[13] V. F. Zimmermann and F. Zimmermann, "Modern and future colliders," Rev. Mod. Phys. **93**, 015006 (2021).

[14] G. Bollen, Y. E. Penionzhkevich, and S. M. Lukyanov, "FRIB – Facility for rare isotope beams," AIP Conf. Proc. **1224**, 432 (2010).

[15] A. Romanenko *et al.*, "Three-dimensional superconducting resonators at $T < 20$ mk with photon lifetimes up to $\tau = 2$ s," Phys. Rev. Appl. **13**, 034032 (2020).

[16] M. K. Transtrum *et al.*, "Superheating field of superconductors within Ginzburg-Landau theory," Phys. Rev. B **83**, 094505 (2011).

[17] N. A. Stilin *et al.*, "CW operation of conduction-cooled Nb_3Sn SRF cavity," paper presented at the 2021 International Conference on RF Superconductivity, 2021.

[18] S. Posen *et al.*, "Advances in Nb_3Sn superconducting radiofrequency cavities towards first practical accelerator applications," Supercond. Sci. Technol. **34**, 025007 (2021).

[19] R. Porter *et al.*, "Progress in Nb3Sn cavities at Cornell University," in North American Particle Accelerator Conference, Lansing, MI, 2019.

[20] U. Pudasaini *et al.*, "Analysis of RF losses and material characterization of samples removed from a Nb_3Sn-coated superconducting RF cavity," Supercond. Sci. Technol. **33**, 045012 (2020).

[21] K. Takahashi *et al.*, "Design and construction of Nb_3Sn vapor diffusion coating system at KEK," in 20th International Conference on RF Superconductivity, Lansing, MI, 2021.

[22] Z. Sun *et al.*, "Smooth, homogeneous, high-purity Nb_3Sn RF superconducting films by seed-free electrochemical synthesis," *arXiv:2302.02054* (2023).

[23] Z. Sun *et al.*, "Surface oxides, carbides, and impurities on RF superconducting Nb and Nb_3Sn: A comprehensive analysis," *arXiv:2305.02467* (2023).

[24] H. H. Farrell, G. H. Gilmer, and M. Suenaga, "Grain boundary diffusion and growth of intermetallic layers: Nb_3Sn," J. Appl. Phys. **45**, 4025 (1974).

[25] H. H. Farrell, G. H. Gilmer, and M. Suenaga, "Diffusion mechanisms for the growth of Nb_3Sn intermetallic layers," Thin Solid Films **25**, 253 (1975).

[26] S.-H. Oh *et al.*, "Diffusion in A15 Nb_3Sn: An atomistic study," Acta Mater. **234**, 118050 (2022).

[27] R. Besson *et al.*, "Atomic-scale study of diffusion in A15 Nb_3Sn," Phys. Rev. B **75**, 054105 (2007).

[28] J. Lee *et al.*, "Atomic-scale analyses of Nb_3Sn on Nb prepared by vapor diffusion for superconducting radiofrequency cavity applications: A correlative study," Supercond. Sci. Technol. **32**, 024001 (2018).

[29] D. L. Hall *et al.*, "Surface analysis of features seen on Nb_3Sn sample coupons grown by vapour diffusion," in International Particle Accelerator Conference, Copenhagen, Denmark, 2017, https://accelconf.web.cern.ch/ipac2017/papers/mopva119.pdf.

[30] R. D. Porter *et al.*, "Update on Nb_3Sn progress at Cornell University," in International Particle Accelerator Conference, Canada, Vancouver, BC, 2018.

[31] U. Pudasaini *et al.*, "Initial growth of tin on niobium for vapor diffusion coating of Nb_3Sn," Supercond. Sci. Technol. **32**, 045008 (2019).

[32] NIST X-ray Photoelectron Spectroscopy Database, Version 4.1 (National Institute of Standards and Technology, Gaithersburg, 2012); http://srdata.nist.gov/xps/.

[33] M. J. Tarlov, J. F. Evans, and J. G. Newman, "Static SIMS and XPS study of water plasma exposed tin oxide films," Appl. Surf. Sci. **64**, 115 (1993).

[34] R. Felix *et al.*, "Preparation and in-system study of $SnCl_2$ precursor layers: Towards vacuum-based synthesis of Pb-free perovskites," RSC Adv. **8**, 67 (2018).

[35] P. Simon *et al.*, "X-ray photoelectronspectroscopy study of passive layers formed on lead-tin alloys," J. Power Sources **52**, 31 (1994).

[36] A. Jain *et al.*, "Commentary: The materials project: A materials genome approach to accelerating materials innovation," APL Mater. **1**, 011002 (2013).